

JGR Solid Earth

RESEARCH ARTICLE

10.1029/2019JB017522

Key Point:

- Kinematic component of earthquake rupture can affect tsunami propagation for long-duration earthquakes

Supporting Information:

- Supporting Information S1

Correspondence to:

A. Williamson,
awillia5@uoregon.edu

Citation:

Williamson, A., Melgar, D., & Rim, D. (2019). The effect of earthquake kinematics on tsunami propagation. *Journal of Geophysical Research: Solid Earth*, 124, 11,639–11,650. <https://doi.org/10.1029/2019JB017522>

Received 8 FEB 2019

Accepted 14 OCT 2019

Accepted article online 24 OCT 2019

Published online 19 NOV 2019

The Effect of Earthquake Kinematics on Tsunami Propagation

A. Williamson¹ , D. Melgar¹ , and D. Rim² 

¹Department of Earth Sciences, University of Oregon, Eugene, OR, USA, ²Department of Applied Physics and Applied Mathematics, Columbia University, New York, NY, USA

Abstract Tsunamis are one of the most destructive effects of subduction zone earthquakes. Directly observing and understanding the generation and propagation of tsunamis remains challenging due to limited offshore instrumentation and a sparse catalog of large events. This makes linking characteristics of the earthquake rupture to their effect on tsunami generation difficult. While past studies explored how varying earthquake source geometries affect tsunami nucleation, little has been done to examine the role of the kinematic component of rupture on the tsunami; we explore these effects in this study. While past studies have examined the kinematic effect using coastal tide gauge data, we expand this examination to more recent pressure gauges. We identify a consistent rotation of the main beam of tsunami energy when using a kinematic model, affecting far-field hazards. We also identify a delay in tsunami arrival times at both coastal and open-ocean gauges that can be as long as the total source duration. For large earthquakes, this delay introduces nonnegligible mapping errors when employing open-ocean tsunami data for source characterizations. As a result of our findings we recommend including a kinematic component to tsunami modeling when studying events with source durations over 120 s and using recordings from open-ocean pressure gauges. We also find that when focusing purely on coastal gauge data and near-source hazards, the kinematic component is a much smaller contribution to the source uncertainty and can be ignored.

1. Introduction

Many of the largest, interplate earthquakes of the past century ruptured over long (>500 km) source lengths, generating tsunamis. For example, the 2004 *M*9.3 Sumatra earthquake had a source length that extended to almost 1,300 km creating a devastating tsunami affecting coastlines throughout the Indian Ocean (Titov et al., 2005). The event had a duration of almost 500 s due to a north propagating unilateral rupture (Ishii et al., 2005). Other large earthquakes including the 1957 *M*8.6 Aleutian Island earthquake, the 1960 *M*9.5 Chile earthquake, the 2010 *M*8.8 Maule earthquake, and the 2011 *M*9.0 Tohoku earthquake ruptured over large length scales (Barrientos & Ward, 1990; Johnson et al., 1994; Ammon et al., 2011; Vigny et al., 2014). Possibly due to the lack of recent large earthquakes coupled with the sparsity in high-quality, historic tsunami observations, the effect that such large sourced and oftentimes long-duration ruptures have on tsunami generation is not clear.

Tsunami data can provide valuable insight into earthquake source processes occurring underwater. The arrival time of the tsunami at a gauge is related to the tsunami source location and the amplitude of the tsunami wave to the scale of deformation. While early use of tsunami data was largely limited to tide gauge recordings and eye witness accounts, this data set has since been supplemented by a suite of offshore pressure gauges and various networks of cabled instruments, providing a richer and near-global view of tsunami propagation. As a direct measurement of the tsunami waves, offshore instrumentation is routinely included in short-term forecasts and tsunami warning projections in the minutes following an earthquake. For large offshore ruptures, tsunami data are also routinely incorporated into finite-fault source characterizations as a supplement to land-based seismic and geodetic data sets (Gusman et al., 2015; Hirata et al., 2006; Melgar & Bock, 2015; Romano et al., 2012; Wei et al., 2011; Williamson et al., 2017; Yue et al., 2014).

The use of these data requires an understanding of how the tsunami waveform is affected by parameters related to the earthquake source. Special attention is placed on the geometric characteristics of the earthquake; varying focal mechanisms, source dimensions, orientations, and depths can all modulate the radiation pattern of tsunami energy (Ben-Menahem & Rosenman, 1972; Geist, 1998; Okal, 1988; Okal et al., 2013). However, the temporal duration of the earthquake rupture, due to both the rupture velocity and

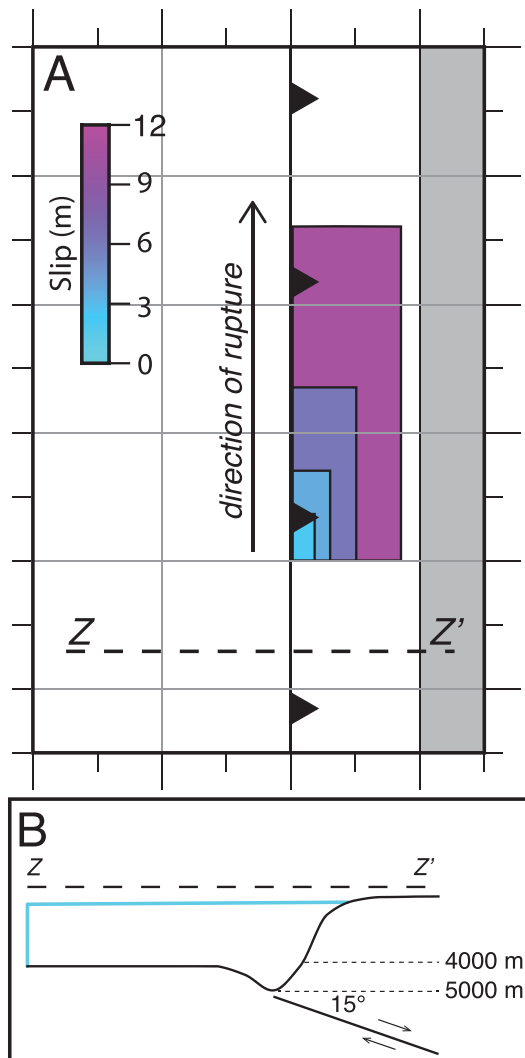


Figure 1. (a) Map view of sandbox model space. Colored boxes indicate the rupture plane for each of the four scenarios. Gray shaded region outlines the coastline. The trench is located west of the fault models. Transect Z to Z' is expanded in panel b. Model space extends an additional 600 km westward from the trench. (b) Trench orthogonal profile of model bathymetry and fault plane.

time windows in tsunami source assessments would be beneficial, both for postevent analysis and tsunami early warning assessment scenarios. We also highlight the spatial uncertainty introduced in finite-fault models, particularly when open-ocean data, which were not yet developed during legacy studies, are used to determine fine-scaled rupture features.

2. Model Setup

2.1. Subduction Geometries and Ruptures

We conduct our analysis using two different model spaces. The first model is a simplified “sandbox” subduction zone, shown in Figure 1, using a flat ocean bottom, a trench, and a gentle slope leading to a linear north-south coastline. Here we also consider only simple homogenous slip source models. We initially use these simplifying assumptions to remove as many sources of uncertainty related to the source and to tsunami propagation as possible in order to isolate effects caused only by the kinematic component of rupture. The second model uses the real bathymetry and fault geometry of the CSZ. Here we also use more complex ruptures

the rupture direction (unilateral, bilateral, etc.), is often ignored when initiating tsunami models. A *static* approximation is usually employed where, for modeling tsunami recordings, the rupture is assumed to be instantaneous. This simplification of the tsunami source stems from past tsunami inversion studies demonstrating that the tsunami propagation speed, which primarily depends on the water column height, is much slower than earthquake rupture speeds (Satake, 1987). For example, a tsunami propagating in the open ocean where the water depth may reach 4,000 m will travel at about 0.2 km/s. This is compared to an earthquake rupture velocity that can range from 1.5–3.0 km/s, a comfortable tenfold increase. However, for the most spatially extensive and temporally long earthquake ruptures, one could question if the common practice of modeling the tsunami as an instantaneous and static source remains valid. Although past studies have addressed this static assumption in tsunami modeling (Kajiura, 1970; Satake, 1987), recent advances in tsunami instrumentation, increases in instrument placement in deep water, and advances in finite fault modeling resolution lead us to reexamine these effects with these modern data sets in mind.

We assess the uncertainty introduced from using a static as opposed to a kinematically rupturing tsunami model for recently developed open-ocean gauges and how it affects the accuracy of earthquake source models and rapid tsunami assessment. We first analyze the role of earthquake rupture duration in the overall tsunami radiation in the near field, focusing on the maximum attained wave heights and arrival time of the tsunami for a range of earthquake sizes using a simplified subduction zone environment devoid of significant path and site effects. We then assess if these same characteristics attributed to a kinematic rupture can be easily identified in more realistic, but noisier, cases using real bathymetry and fault geometries for the Cascadia Subduction Zone (CSZ). The use of simple and then more complex, yet synthetic, environments helps us to identify trends that may be apparent in real data without the additional uncertainty related to unknowns in source processes.

We are particularly interested in the impact that a kinematic rupture on a long interplate fault would have on tsunami early warning and rapid fine-scaled coseismic slip characterizations such as tsunami arrival time and maximum amplitude. Therefore, we study the tsunami as it propagates toward the far field and deep-ocean pressure gauges, often used in early warning, as well as toward the coastline and tide gauges. With this information, we make recommendations on when the inclusion of multiple-

on the CSZ. In this way we introduce tsunami path and site effects from irregular bathymetry. Stochastic slip distributions also lead to complex coastal tsunami amplitude patterns and arrival times. Since we are interested in the most extreme cases, we maintain largely unilateral ruptures for both the sandbox and CSZ examples for the sake of comparison.

For the simple sandbox case we run both a kinematic and a static model for four different magnitudes for a total of eight rupture scenarios. Each rupture occurs on the simulated plate interface with a fixed strike of 0° (parallel to the trench) and a 15° dip. The length and width of each fault plane is determined through the empirical scaling relations for low angle thrusts in subduction zone environments as recorded in Blaser et al. (2010) and documented in supporting information Table S1. We assign a homogenous slip scaled to the appropriate magnitude for each case.

Rupture is treated as instantaneous for the static cases. This means the seafloor over the entire rupture area deforms at the first time step. Rupture in the kinematic cases has a finite duration meaning that the seafloor deformation that initiates the tsunami propagation is distributed over multiple time steps. For each of the four kinematic cases, rupture initiates at the epicenter which is located midway down the fault width at the southern edge of the fault plane. The rupture propagates unilaterally from the epicenter to the north with a constant rupture velocity of 2.0 km/s . The total rupture duration for each scenario is scaled to the fault dimensions which depend on the magnitude (Figure S1).

Rupture scenarios along the plate interface of the CSZ use a slab geometry based on crustal surveying from McCrory et al. (2012) as used as a supplement to the global Slab 2.0 model (Hayes et al., 2018). The slab geometry is then discretized into a triangular mesh to account for the variability of strike and dip over the region. Both static and kinematic ruptures are tested for two scenarios: a small rupture over a central segment of the CSZ and a large rupture that extends over the majority of the CSZ. The large rupture approximates the extent of slip from the 1700 earthquake as modeled by Satake et al. (2003).

Both ruptures are largely unilateral, using synthetic Cascadia earthquakes from the catalog of Melgar et al. (2016). These slip distributions for these events, which are used to generate the seafloor deformation that then initiates the tsunami propagation, are created using the Karhunen-Loëve expansion method described in Melgar et al. (2016) for Cascadia specific cases and more generally in LeVeque et al. (2016). This method assigns slip over each subfault using a von Karman correlation function, which has been found to best describe the slip distributions from past finite-fault solutions of moderate sized earthquakes (Mai & Beroza, 2002). The catalog of Melgar et al. (2016) includes over 1,300 kinematic slip models ranging in magnitude from $M7.8$ to $M9.2$, we have selected for our purposes two unilateral rupturing examples, a large $M8.95$ event and a smaller $M8.26$ earthquake.

2.2. Tsunami Modeling

The deforming seafloor initiates the tsunami propagation model. Seafloor deformation at each time step during rupture is calculated through the superposition of angular dislocations for triangular faults in an elastic half space (Comninou & Dundurs, 1975). This is an adaptation from the traditional Okada equations that consider rectangular faults (Okada, 1985). We use the triangular component so that our subfaults, particularly in the geometrically more complex Cascadia examples, can vary in strike and dip without overlap. We assume an incompressible water column, allowing us to translate the seafloor deformation to a disturbance at the sea surface. Both the deformation and the tsunami are modeled using the GeoClaw software package, which solves the two-dimensional depth-averaged nonlinear shallow water equations (LeVeque et al., 2011). We treat the edge of the model domain as a nonreflective boundary. GeoClaw also allows the wet/dry boundary of the coastline to oscillate as the tsunami makes landfall.

We simulate a tsunami for each of the sandbox models over 3 hr of propagation time. The model over the Cascadia subduction zone requires 6 hr of propagation time for the tsunami to traverse the entire model domain. We initiate the kinematic component of our tsunami model with a 1 s time step over the duration of the rupture (which is typically between 0.5 and 5 min). After the initial generation stage, the remaining tsunami propagation uses a time step that varies to fit a preset desired Courant-Friedrichs-Lowy value of 0.75. In order to model the tsunami over a rupture duration, the time step needs to be set initially low.

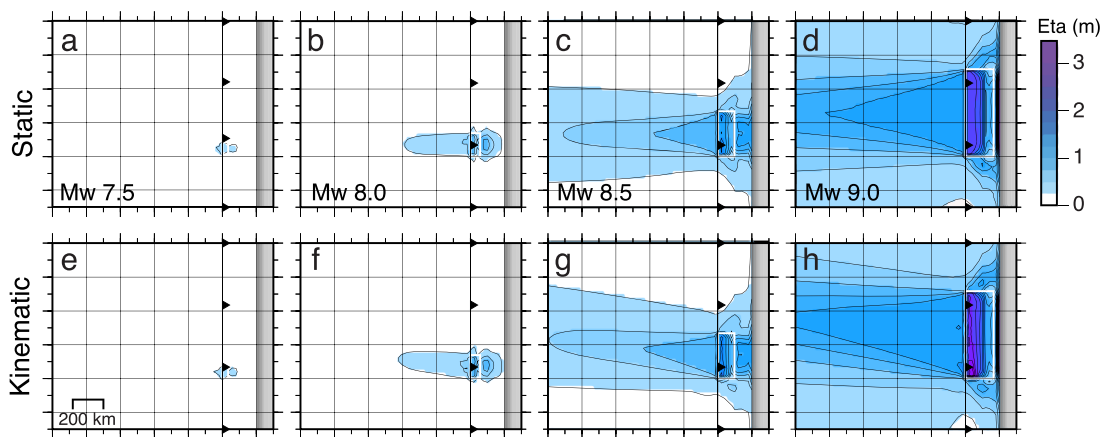


Figure 2. Maximum wave height for all eight ruptures. (a–d) The maximum wave height for the static rupture of each magnitude. (e–h) The maximum wave height for the kinematic rupture of each magnitude. For each kinematic case, the rupture front starts at the southern end and propagates unilaterally to the north. Gray shaded region in each subplot is land. The fault geometry is outlined in white. Black line with east pointing hatches marks trench.

3. Model Results

3.1. Sandbox Case: Amplitudes

Typically, a quick approximation of a tsunami's size and therefore the hazard that it poses to coastlines is made by analyzing the amplitude of the tsunami as it passes over deep-ocean pressure and coastal tide gauges. These are recordings at specific points within the larger-scale tsunami radiation pattern. For small tsunamis, this radiation pattern may remain local, but for tsunamis that are generated from earthquakes with magnitudes exceeding $M8.5$, it is possible to measure the tsunami with appreciable amplitudes at trans-oceanic distances. It is important to note that while a general case can be made that the size of a tsunami scales with the size of an earthquake, there are exceptions. Here, we assess how treating a tsunami as a kinematic rupture changes the overall tsunami radiation when compared to the static case.

The radiation of tsunami energy for each of the eight sandbox model scenarios is shown in Figure 2. Each of the four static rupture cases show essentially the same open-ocean pattern but scaled to an increasing magnitude. The area with the largest maximum wave amplitude in the offshore direction is directed perpendicular to the strike of the fault plane. Areas oblique to the fault plane have substantially lower wave amplitudes. This is consistent with the description of tsunami wave directivity from Okal et al. (2013) and Ben-Menahem and Rosenman (1972) for a purely thrust event as well as descriptions made by Carrier and Yey (2010). The wave amplitude in the direction of the coastline is greatest alongside the rupture length, decaying as the distance from the edge of the fault increases.

In the kinematic scenarios, where rupture is unilateral and south to north, the main direction of maximum wave height in the offshore direction is not perpendicular to the fault strike, as was seen in the static cases. Instead, the main beam of energy is rotated from perpendicular in the direction of rupture propagation. In the case provided here where the rupture velocity is fixed at 2 km/s, the amount of rotation is about 5° .

The degree of rotation between static and kinematic cases for a unilateral rupturing case, like those modeled here, is dependent on the rupture velocity. A slower rupture velocity amounts to a greater rotation, while a faster rupture amounts to a smaller rotation. The degree of rotation from perpendicular for a rectangular fault, constant rupture velocity, and flat bathymetry is

$$d_{\text{rot}} = \tan^{-1} \left(\frac{T_R \sqrt{gH}}{L} \right) \quad (1)$$

where T_R is the total rupture duration, g is acceleration due to gravity, H is water column depth, and L is the fault length. Because the static case is equivalent to an instantaneous rupture, the rupture velocity approaches infinity (Figure S2) and d_{rot} is 0° .

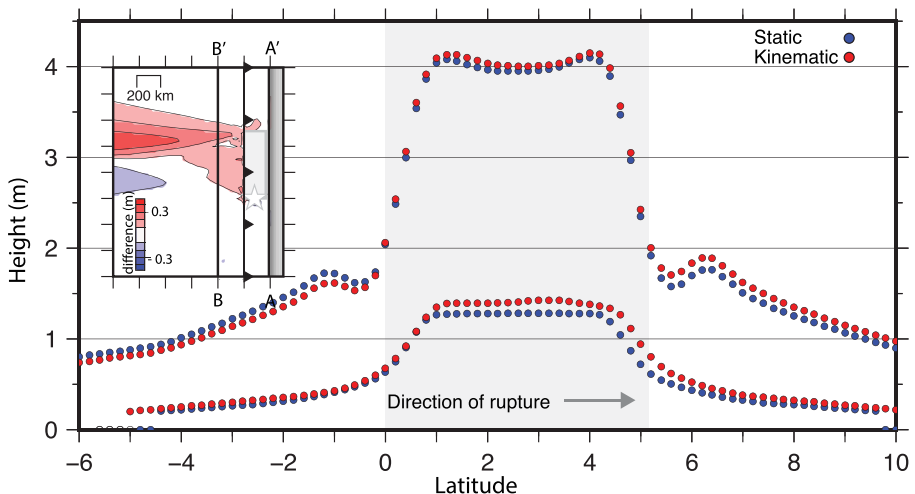


Figure 3. Coastal amplitudes for kinematic (red) and static (blue) points along two transects for an M_9 earthquake. Transect A-A' is located at the coastline, and transect B-B' is located 200 km from the trench in the offshore direction. Shaded box indicates latitude range of the fault. (inset) Difference between kinematic and static offshore tsunami amplitude patterns. Areas shaded red indicate an increase in amplitude, while areas shaded in blue indicate a decrease. Unshaded areas have difference of less than 10 cm. Solid black lines indicate the locations of transects A-A' and B-B', shown in main figure. Star shows the epicenter of the earthquake, used as the starting point for rupture in the kinematic model.

While this rotation seems small and does not play a large impact in tsunami hazard assessment for the near field, it has a significant impact on tsunami directivity in the far field where a small rotation over the span of thousands of kilometers yields a greater offset. Outside of the rotation, the absolute value of the maximum amplitude toward the far field is not affected by the inclusion of rupture kinematics, as shown in the inset of Figure 3.

In the near field and along the coastline, the difference in tsunami amplitude between static and kinematic cases is small, as illustrated in Figure 3 where transects of the amplitude are plotted for the most extreme $M_{9.0}$ cases. Leeward from the rupture, amplitudes from the kinematic rupture are slightly lower than the static one and are slightly larger in the direction of rupture. However, the difference along the coastline amounts to less than 10 cm (or about 2% of the peak amplitude) between the two cases. This is near negligible on a rupture with a maximum wave height as the wave approaches the coast of over 4 m. A transect 200 km in the offshore direction shows a similarly small change between the two models. This distance was chosen because it is a typical distance that offshore pressure gauges, like new generation Deep Ocean Assessment and Reporting of Tsunami (DART) 4G buoys reside.

3.2. Sandbox Case: Arrival Times

In addition to amplitude, changes to the arrival time of a tsunami at the coast or at offshore gauges should also be considered. For both warning and science applications waveform data recorded at gauges is used to map the starting point of deformation, based on when the tsunami arrived at the gauge and by making assumptions about its propagation path. Here, the arrival of the tsunami is defined as the point in time when the water column height at a point of interest rises by more than 10 cm for the first time. This provides a consistent reference for comparing each scenario. If a gauge never records an increase greater than or equal to this threshold, then the area is defined as not being affected by the tsunami.

The arrival times along the coast as well as along offshore transects in the near field are shown in Figure 4. Because of the assumption of an instantaneous deformation over the entire fault at the first time step, the tsunami arrival at gauges in the static case always represents the earliest arrival time possible. Arrival times in the kinematic case are almost always later and depend on the location of the gauge in reference to the fault rupture. Figure 4 shows the kinematic delay observed at points located along the coastline and at 200 km seaward of the trench for the $M_w 9.0$ sandbox scenarios. The coastal arrival time

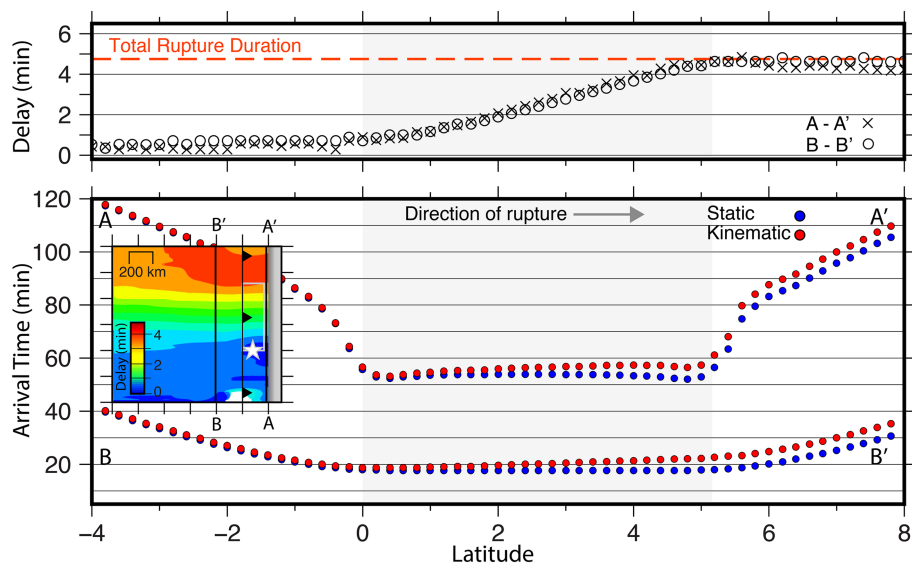


Figure 4. (bottom) Tsunami arrival times for kinematic (red) and static (blue) points along two transects for an M9 earthquake. Transect A-A' is located at the coastline, and transect B-B' is located 200 km from the trench in the offshore direction. Shaded box indicates latitude range of the fault. (inset) Difference between kinematic and static arrival times over near-field region. Solid black lines indicate the locations of transects A-A' and B-B', shown in main figure. Star shows the epicenter of the earthquake, used as the starting point for rupture in the kinematic model. (top) Delay between kinematic and static arrival times for transect A-A' (crosses) and B-B' (open circles). Dashed line marks the total rupture duration in minutes.

of the tsunami south of the fault plane (away from the direction of rupture) shows no delay between the kinematic and static scenarios. The coast in line with the fault plane has a delay that increases with distance in the direction of rupture. North of the rupture plane, the delay is consistent and equal to the total rupture duration for this case (190 s). We observed the same kinematic effect for each of the four magnitude scenarios, scaled to the rupture duration. Each of these cases shows a purely unilateral rupture. For a bilateral rupture, small delays may be observed in both directions relative to the fault plane, and for increasingly complex rupture fronts, the amount of delay observed over the coastline will be increasingly complex.

3.3. Sandbox Case: Summary

From these sandbox models, we show that kinematic rupture redistributes tsunami energy through a rotation in the direction of rupture. This degree of rotation depends primarily on the rupture velocity and affects the impact of tsunami directivity in the far field and consequently the use of far-field stations. Along the coast, a one-to-one comparison of tsunami amplitude shows a small difference between the two models amounting to less than 2% of the maximum observed coastal amplitude. We also illustrate that the rupture duration affects the tsunami arrival time. The difference in arrival between static and kinematic cases at any gauge depends on the gauge's location in reference to the rupturing fault: Gauges away from the direction of rupture are not impacted, but gauges past the rupture see differences which can be as large as the total rupture duration. This difference in modeled arrival time affects tsunami source placement and is a source of error in earthquake source characterization.

4. Realistic Examples: The CSZ

The sandbox case intentionally excludes details that are common when modeling real tsunamis, including complex coastlines, irregular bathymetry, and heterogeneous ruptures. Here we introduce more realistic effects and extend the analysis to include two tests focusing on the CSZ. We focus on this location because of its well-documented history of producing large tsunamigenic earthquakes (Atwater, 1992; Witter et al., 2003) like the ~M9 1700 earthquake that extended from northern California through Vancouver Island, Canada (Atwater et al., 1995; Satake et al., 2003). Additionally, geodetic coupling models (Schmalzle

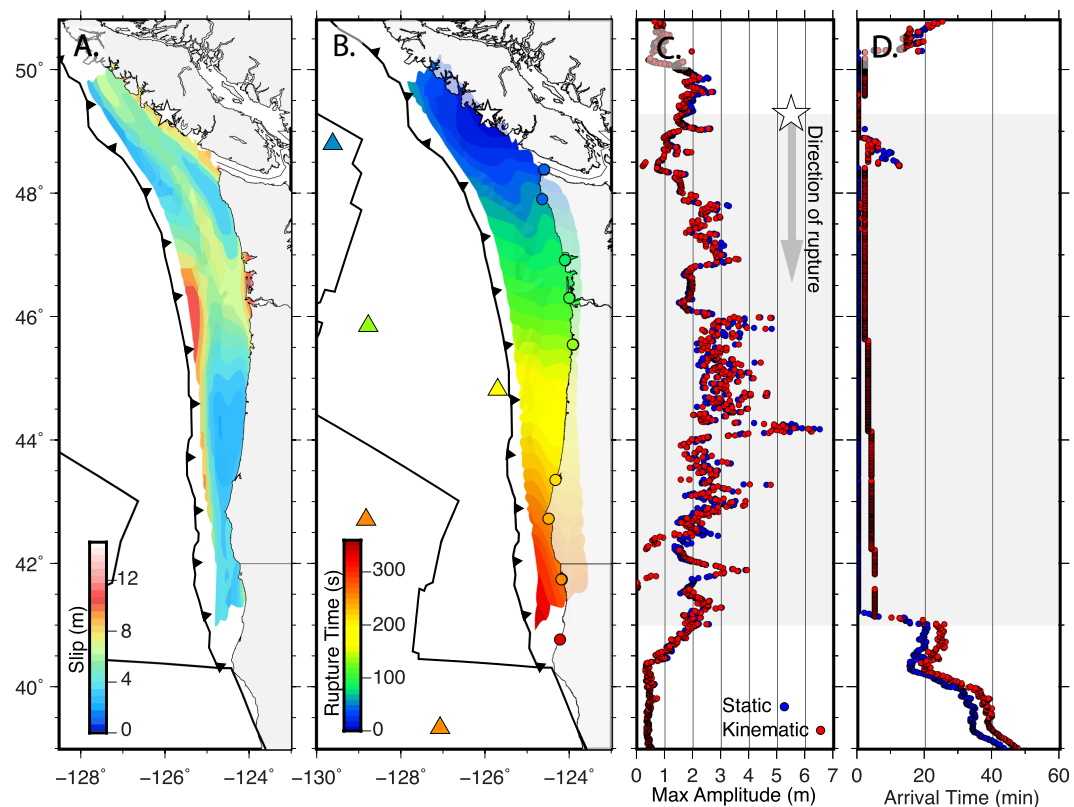


Figure 5. Comparison of static and kinematic ruptures for the full rupture of the CSZ. (a) Initial stochastic slip distribution. (b) Onset of rupture along the fault plane. White star in panels a and b indicates the epicenter of the rupture. (c) Maximum recorded amplitude along the Cascadia coastline for static (blue) and kinematic (red) models. Gray shaded region shows latitude range of the rupture plane. Star and gray arrow show the start and direction of the majority of the rupture. (d) Tsunami arrival time, in minutes, for static and kinematic cases over the same latitude range as panel c.

et al., 2014) and the lack of large seismicity on the plate interface over the modern era suggest a high likelihood of future large event that likely would generate a tsunami. Furthermore, given the significant length of the plate boundary (~1,100 km), unilateral ruptures with significant kinematic effects are possible.

The first CSZ model, shown in Figure 5, uses a stochastic slip distribution that extends over most of the available model space. The model replicates a M_w 8.95 with up to 10 m of shallow slip on the plate interface and a rupture that initiates in the north and ruptures nearly unilaterally toward the south with a total rupture duration of 350 s. The length scale of this example emulates the expected rupture length of the 1700 Cascadia earthquake as modeled by Satake et al. (2003). We record the expected tsunami at the locations of currently deployed DART gauges and National Oceanic and Atmospheric Administration tsunami-capable coastal tide gauges. This is in addition to a dense transect of synthetic coastal observation points. While the expected effect of the kinematic component of rupture on the arrival time and amplitude is clear from the sandbox case, the use of realistic data sets will help to determine if the added complexity of using realistic geometries can overshadow these effects.

The maximum amplitude, along the coastline, for both kinematic and static cases is similar. The average percent difference between the two sets is 5.5%, while the maximum observed coastal amplitude is 6.5 m. The overall distribution of amplitudes is more complex than in the sandbox cases with some areas seeing localized concentrations of energy. This is due to the stochastic slip distribution, an irregular coastline that can concentrate energy into bays, and real bathymetry that can also channel the tsunami toward the coastline, for example, in Crescent City in northern California (Horrillo et al., 2008).

With the introduction of model complexities, the coastal amplitudes between static and kinematic cases do not show a systematic pattern as in the simpler sandbox case. However, despite the added model

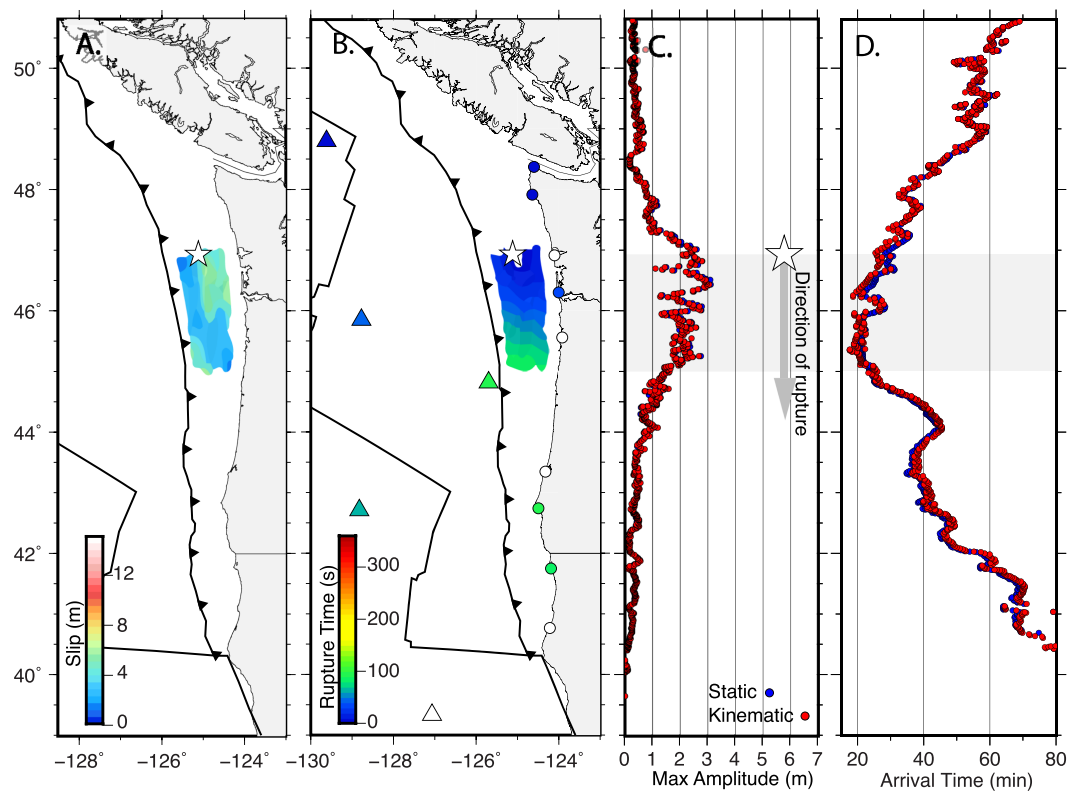


Figure 6. Comparison of static and kinematic ruptures for a segment rupture of the CSZ. (a) Initial stochastic slip distribution. (b) Onset of rupture along the fault plane. (c) Maximum recorded amplitude along the Cascadia coastline for static (blue) and kinematic (red) models. (d) Tsunami arrival time, in minutes, for static and kinematic cases over the same latitude range as panel c.

complexities, the tsunami arrival at the same coastal and open-ocean DART locations clearly show the growing delay in arrival time, for the kinematic case, in the main direction of rupture. Like in the sandbox case, this delay persists as a constant offset past the rupture plane and affects both near-shore and open-ocean recordings. The maximum temporal offset in this example, as measured at the end of the rupture, is 5.5 min.

Figure 6 examines the same coastal properties but for a smaller rupture. Here, only a segment of the CSZ ruptures in a Mw 8.26 with a maximum slip of 6 m and a total rupture duration of 90 s. Just as in the larger rupture scenario shown previously, there is little difference in maximum coastal amplitude. However, even with a shorter rupture and smaller magnitude event, there is still a clear pattern to the delay in tsunami arrival at the four nearest DART gauges. As will be discussed in the following section, this has implications for the veracity of tsunami source modeling.

5. Discussion

The two characteristics of tsunami propagation that are affected by the choice in rupture modeling are the far-field directivity of the tsunami and the tsunami arrival time at coasts and open-ocean gauges. We will first discuss the implications of the change in directivity and how this affects the use of far-field stations in source analysis as well as far-field warning assessments. Then we illustrate how tsunami arrival times affect source modeling and why this is a departure from previous studies such as Satake (1987).

Observations of tsunami amplitudes are often used as a quick assessment of the overall tsunami hazard affecting coastal communities in real time. When focusing purely on the effect of a kinematic rupture, the maximum tsunami amplitude at near-field gauges does not largely change. While the sandbox examples saw differences amounting to about 2% of the maximum amplitude, these differences are not apparent

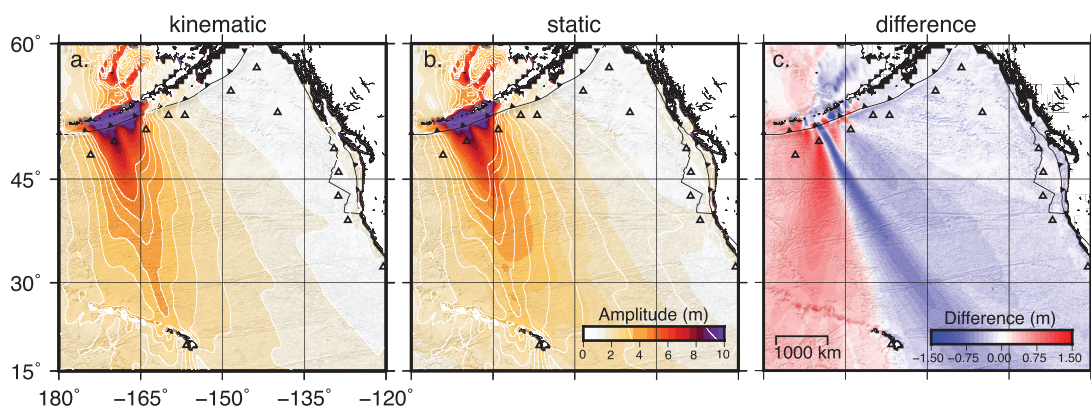


Figure 7. Extent of a rotation in tsunami energy directivity for far-field sites from a heterogeneously slipping event on the Aleutian Islands. (a) Amplitude distribution using a unilateral rupture (east to west) and a rupture velocity of 1.5 km/s. (b) Amplitude distribution using an instantaneous rupture. White contours to compare the pattern of the kinematic open-ocean amplitudes on the static event. (c) Difference in amplitude between the kinematic and static models. Black triangles indicate locations of currently deployed DART buoys.

once model complexities are introduced. Some studies of low rupture velocities and long rise times do, however, see an increase in total run-up amplitudes on simple sloping shorelines in a model environment (Fuentes et al., 2018). However, it is also possible that increased run-ups during these events are due to anelastic deformation of the shallow wedge (e.g. Ma, 2012).

We do advocate that the kinematic component makes a difference in tsunami propagation toward the far field, primarily due to the direction of the tsunami's radiation pattern, which depends on rupture velocity. In the static case using pure thrust, the main region with high maximum tsunami amplitudes is concentrated in a beam perpendicular to the strike of the fault plane. In the kinematic cases, also using pure thrust, this main beam of high amplitude is rotated in the same direction as the rupture front. Observed rotations over a range of rupture velocities vary between 0° and 8°; in the near field, this amounts to an offset on a scale of only tens of kilometers, which would likely go unnoticed given the significance of the impacts. However, for a large tsunami that propagates over thousands of kilometers, this offset can grow to several hundreds of kilometers in the far field. With a DART gauge spacing of hundreds of kilometers, the ability of rapidly accounting for the initial deformation from the output of one or maybe two gauges is compromised for large rotations (slow rupture velocities). For tsunami warning systems, this can affect how warnings and forecasts are handled for far-field locations which can still receive damage from large transoceanic events.

To illustrate this, consider an earthquake and tsunami originating along the Aleutian Islands as shown in Figure 7. The tsunami's amplitude in the far field varies between a kinematic and a static model; with increasing distance, the offset of waves >3 m is almost 1,000 km. This has implications on how middle- to far-field localities, like the Hawaiian Islands, are affected. Compared to the static case, a slow rupture can rotate energy completely away from the island chain. This example is particularly relevant as the tsunami generated from the 1946 Aleutian Island earthquake, which affected Hawaii with little warning, led to a large number of casualties. The destruction from this event and its lack of warning was the impetus for the creation of the first of two U.S. tsunami warning centers (Bernard & Titov, 2015). Since the warning centers' creations, our understanding and modeling abilities of tsunamis has vastly increased.

This far-field rotation can also affect earthquake source modeling. If using tsunami instrumentation located near Hawaii to look at the Aleutian source, the difference in where the highest amplitude is observed at the gauges affects the location of slip on the fault depending on whether an instantaneous or kinematic model is used. The addition of rupture kinematics is important to further refine our understanding of how near- and far-field communities alike are impacted from tsunamis and for forecasts to be as useful and precise as possible. This is true for earthquake prone regions where middle-distance (~1,000 km) off-shore instrumentation is sparse, leading us to rely on only near-field data to make far-field forecasts. In addition to the Aleutian Islands affecting Hawaii, this includes earthquakes originating on the

Peru-Chile trench affecting Australia, and the Sunda megathrust affecting the east coast of Africa and the Indian subcontinent.

We also advocate that the temporal effect is important, particularly for fine-scaled finite-fault models of large earthquakes. The arrival time of the tsunami at a gauge is directly related to the location of slip on the fault plane. A difference in arrival time of 1 min to a pressure gauge changes the location of slip. The spatial offset of this change is dependent on the tsunami's propagation velocity from the source location and arrival time at gauges. The difference in arrival time of the tsunami at gauges between static and kinematic cases is dependent on the earthquake rupture velocity, the rupture duration, and the location of the gauge in relation to the rupture front. Gauges located in the direction opposite of the propagating rupture front and away from the fault plane see no delay. Conversely, gauges past the fault in the direction of rupture see delays that can be as large as the total rupture duration. For large earthquakes, this delay can reach multiple minutes and is prevalent at both near-coastal and open-ocean sites. The delay was clear in the sandbox case and even with the inclusion of real coastlines, bathymetries, and stochastic slip models in the CSZ models.

This delay of seconds to minutes affects our understanding of the earthquake source. For sources located near the trench of subduction zones, where the water column depth ranges exceed 1,000 m (where tsunamis propagate faster), a delay time of multiple minutes can contribute to tens of kilometers of spatial offset. If using a finite-fault model with a coarse fault discretization ($>50 \times 50$ km patches) an offset of this distance will likely not affect model results. However, a patch size that is smaller than these distances will see different model results depending on whether a static or multiple time window inversion is used. Sources where the tsunami is generated closer to the shoreline will not see as large a spatial offset.

It is important to note that there have been a few studies that do incorporate rupture velocity or multiple time windowed inversion methods when handling tsunami data. To highlight a few examples, Fujii and Satake (2007) included a rupture velocity component to their tsunami and satellite altimetry joint inversion of the 2004 Sumatra earthquake. The study varied the rupture velocity from 0.5 to 3.0 km/s when modeling slip over 22 equally sized 100 by 100 km subfaults. In this case the rupture velocity component had little effect on the inversion results. However, the large subfault size also inhibits any differences, even for the long duration of this event. A similar analysis of the same earthquake was also completed by Tanioka et al. (2006) using five regional tide gauges, Piatanesi and Lorito (2007) with 14 stations, and Hirata et al. (2006) with satellite altimetry. Satake et al. (2013) updated a prior assessment of the 2011 Tohoku earthquake to include a multiple time window inversion using a combination of local tide gauges, GPS wave gauges, cabled ocean bottom pressure gauges, and near-field open-ocean DART. The inclusion of a multi-time window approach was motivated by the inclusion of previously unavailable high-rate and local data. They use a mix of coarse 50 by 50 km subfaults and smaller 25 by 50 km subfaults for the intermediate and shallow portions of the fault, respectively. The authors of this study identified the difference in arrival time at certain tide gauges between instantaneous and delayed rupture models. Hossen, Cummins, Dettmer et al. (2015) and Hossen, Cummins, Robert, et al. (2015) also analyzed the tsunami of the Tohoku earthquake, building on Satake et al. (2013) by including dispersion. Gusman et al. (2015) used multiple time windows to look at the Iquique, Chile, earthquake. Ho et al. (2019) assessed if a multiple time window inversion would provide added insight to the 1960 Chile earthquake; however, all tsunami sensors used were located opposite of the direction of rupture. While these studies use multiple-time window approaches, we identify the root cause and prevalence of the delay that these methods aim to correct. We also shed light on what spatial scale these methods hold most value. For example, even the most robust analysis on rupture velocity has limited impact when only coarse subfaults are used. In the case of fine-scaled (< 20 by 20 km) subfault scenarios a check on the role of rupture velocity is important.

6. Conclusions and Recommendations

Over the past decade, the number of deployed open-ocean gauges has increased. Coupled with stronger computational power, tsunami source characterization is constantly improving by means of more accurate time variable and fine scaled earthquake rupture models. For earthquakes that rupture over long source dimensions and with long rupture durations, the common approximation of the tsunami being generated instantaneously from a static deformation becomes less valid. The main impacts from the static assumption are delays as large as the earthquake rupture duration (which can be multiple minutes for large magnitude

events) observed at coastal and open-ocean gauges and a miscalculation in far-field tsunami hazard due to ignoring rupture velocity-driven beam rotation. As earthquake source models become more advanced and reliably take into account more diverse data sets that include tsunami gauge data, we recommend the following guidelines for optimal source characterizations:

1. The uncertainty in tsunami directivity that is introduced by rupture velocity should be considered when a tsunami is generated that is expected to affect coastlines at far-field (>2,000 km) distances. Depending on the rupture velocity, beam rotations nearing 10° are possible, which can impact far-field forecasting and source inversions.
2. The direction of rupture impacts the arrival time of the tsunami at gauges in that same direction while leaving gauges on the lee side unaffected. This means that the spatial effect of a kinematic as opposed to static approximation is variable.
3. The water column depth at the tsunami source location contributes to a spatial uncertainty when ray tracing the tsunami from open-ocean pressure and coastal tide gauges. The greater the depth at the source, the larger the potential offset between slip placement for kinematic and static finite fault inversions using tsunami waveform data. Caution should be used when modeling near-trench deeper water sources compared to sources near the coastline where the water column is shallower.

While earthquake ruptures can include countless complexities that deviate from the unilateral cases shown in this study, the inclusion of these recommendations in the decision-making tree for rapid characterizations as well as detailed postevent finite fault studies will help to better integrate tsunami data for long-duration events.

Acknowledgments

We thank Randall LeVeque for his helpful comments on this manuscript. This work was funded in part by NASA Grant 18-RRNES18-0001. The stochastic slip models used in this study are publicly available from <https://zenodo.org/record/59943>, the code that generates them can be obtained from <https://github.com/dmelgarm/MudPy>, and a tutorial on how to generate the slip models is available online (from [https://github.com/dmelgarm/MudPy/wiki/Stochastic-slip-\(fakequakes\)](https://github.com/dmelgarm/MudPy/wiki/Stochastic-slip-(fakequakes))). The Clawpack/Geoclaw tsunami modeling code is openly available online (at <http://www.clawpack.org/>). We also would like to thank three anonymous reviewers whose recommendations have strengthened this manuscript.

References

- Ammon, C. J., Lay, T., Kanamori, H., & Cleveland, M. (2011). A rupture model of the 2011 off the Pacific coast of Tohoku earthquake. *Earth, Planets and Space*, 63(7), 33.
- Atwater, B. F. (1992). Geologic evidence for earthquakes during the past 2000 years along the Copalis River, southern coastal Washington. *Journal of Geophysical Research*, 97(B2), 1901–1919. <https://doi.org/10.1029/91JB02346>
- Atwater, B. F., Nelson, A. R., Clague, J. J., Carver, G. A., Yamaguchi, D. K., Bobrowsky, P. T., et al. (1995). Summary of coastal geologic evidence for past great earthquakes at the Cascadia subduction zone. *Earthquake Spectra*, 11(1), 1–18. <https://doi.org/10.1193/1.1585800>
- Barrientos, S. E., & Ward, S. N. (1990). The 1960 Chile earthquake: Inversion for slip distribution from surface deformation. *Geophysical Journal International*, 103(3), 589–598. <https://doi.org/10.1111/j.1365-246X.1990.tb05673.x>
- Ben-Menahem, A., & Roseman, M. (1972). Amplitude patterns of tsunami waves from submarine earthquakes. *Journal of Geophysical Research*, 77(17), 3097–3128. <https://doi.org/10.1029/JB077i017p03097>
- Bernard, E., & Titov, V. (2015). Evolution of tsunami warning systems and products. *Philosophical Transactions of the Royal Society A: Mathematical, Physical and Engineering Sciences*, 373(2053), 20140371.
- Blaser, L., Krüger, F., Ohrnberger, M., & Scherbaum, F. (2010). Scaling relations of earthquake source parameter estimates with special focus on subduction environment. *Bulletin of the Seismological Society of America*, 100(6), 2914–2926. <https://doi.org/10.1785/0120100111>
- Carrier, G. F., & Yey, H. (2010). Tsunami propagation, directivity, and pulse persistence from a finite source. In *Water Waves: Theory*
- Comninou, M., & Dundurs, J. (1975). The angular dislocation in a half space. *Journal of Elasticity*, 5(3-4), 203–216. <https://doi.org/10.1007/BF00126985>
- Fuentes, M., Riquelme, S., Ruiz, J., & Campos, J. (2018). Implications on 1+1 D tsunami runup modeling due to time features of the earthquake source. *Pure and Applied Geophysics*, 175(4), 1393–1404. <https://doi.org/10.1007/s0024-018-1804-2>
- Fujii, Y., & Satake, K. (2007). Tsunami source of the 2004 Sumatra–Andaman earthquake inferred from tide gauge and satellite data. *Bulletin of the Seismological Society of America*, 97(1A), S192–S207. <https://doi.org/10.1785/0120050613>
- Geist, E. L. (1998). Local tsunamis and earthquake source parameters. *Advances in Geophysics* (Vol. 39, pp. 117–209).
- Gusman, A. R., Murotani, S., Satake, K., Heidarzadeh, M., Gunawan, E., Watada, S., & Schurr, B. (2015). Fault slip distribution of the 2014 Iquique, Chile, earthquake estimated from ocean-wide tsunami waveforms and GPS data. *Geophysical Research Letters*, 42, 1053–1060. <https://doi.org/10.1002/2014GL062604>
- Hayes, G. P., Moore, G. L., Portner, D. E., Hearne, M., Flamme, H., Furtney, M., & Smoczyk, G. M. (2018). Slab2, a comprehensive subduction zone geometry model. *Science*, 362(6410), 58–61. <https://doi.org/10.1126/science.aat4723>
- Hirata, K., Satake, K., Tanioka, Y., Kuragano, T., Hasegawa, Y., Hayashi, Y., & Hamada, N. (2006). The 2004 Indian Ocean tsunami: Tsunami source model from satellite altimetry. *Earth, Planets and Space*, 58(2), 195–201. <https://doi.org/10.1186/BF03353378>
- Ho, T. C., Satake, K., Watada, S., & Fujii, Y. (2019). Source estimate for the 1960 chile earthquake from joint inversion of geodetic and transoceanic tsunami data. *Journal of Geophysical Research: Solid Earth*, 124(3), 2812–2828.
- Horrillo, J., Knight, W., & Kowalik, Z. (2008). Kuril Islands tsunami of November 2006: 2. Impact at Crescent City by local enhancement. *Journal of Geophysical Research*, 113, C01021. <https://doi.org/10.1029/2007JC004404>
- Hossen, M. J., Cummins, P. R., Dettmer, J., & Baba, T. (2015). Tsunami waveform inversion for sea surface displacement following the 2011 Tohoku earthquake: Importance of dispersion and source kinematics. *Journal of Geophysical Research: Solid Earth*, 120, 6452–6473. <https://doi.org/10.1002/2015JB011942>
- Hossen, M. J., Cummins, P. R., Roberts, S. G., & Allgeyer, S. (2015). Time reversal imaging of the tsunami source. *Pure and Applied Geophysics*, 172(3-4), 969–984. <https://doi.org/10.1007/s0024-014-1014-5>

- Ishii, M., Shearer, P. M., Houston, H., & Vidale, J. E. (2005). Extent, duration and speed of the 2004 Sumatra–Andaman earthquake imaged by the Hi-Net array. *Nature*, 435(7044), 933–936. <https://doi.org/10.1038/nature03675>
- Johnson, J. M., Tanioka, Y., Ruff, L. J., Satake, K., Kanamori, H., & Sykes, L. R. (1994). The 1957 great Aleutian earthquake. In *Shallow subduction zones: Seismicity, mechanics and seismic potential* (pp. 3–28). Basel: Birkhäuser.
- Kajura, K. (1970). 45. Tsunami source, energy and the directivity of wave radiation.
- LeVeque, R. J., George, D. L., & Berger, M. J. (2011). Tsunami modelling with adaptively refined finite volume methods. *Acta Numerica*, 20, 211–289. <https://doi.org/10.1017/S0962492911000043>
- LeVeque, R. J., Waagan, K., González, F. I., Rim, D., & Lin, G. (2016). Generating random earthquake events for probabilistic tsunami hazard assessment. In *Global tsunami science: Past and future* (Vol. I, pp. 3671–3692). Cham: Birkhäuser.
- Ma, S. (2012). A self-consistent mechanism for slow dynamic deformation and tsunami generation for earthquakes in the shallow subduction zone. *Geophysical Research Letters*, 39, L11310. <https://doi.org/10.1029/2012GL051854>
- Mai, P. M., & Beroza, G. C. (2002). A spatial random field model to characterize complexity in earthquake slip. *Journal of Geophysical Research*, 107(B11), 2308. <https://doi.org/10.1029/2001JB000588>
- McCrory, P. A., Blaier, J. L., Waldhauser, F., & Oppenheimer, D. H. (2012). Juan de Fuca slab geometry and its relation to Wadati–Benioff zone seismicity. *Journal of Geophysical Research*, 117, B09306. <https://doi.org/10.1029/2012JB009407>
- Melgar, D., & Bock, Y. (2015). Kinematic earthquake source inversion and tsunami runup prediction with regional geophysical data. *Journal of Geophysical Research: Solid Earth*, 120, 3324–3349. <https://doi.org/10.1002/2014JB011832>
- Melgar, D., LeVeque, R. J., Dreger, D. S., & Allen, R. M. (2016). Kinematic rupture scenarios and synthetic displacement data: An example application to the Cascadia subduction zone. *Journal of Geophysical Research: Solid Earth*, 121, 6658–6674. <https://doi.org/10.1002/2016JB013314>
- Okada, Y. (1985). Surface deformation due to shear and tensile faults in a half-space. *Bulletin of the Seismological Society of America*, 75(4), 1135–1154.
- Okal, E. A. (1988). Seismic parameters controlling far-field tsunami amplitudes: A review. *Natural Hazards*, 1(1), 67–96. <https://doi.org/10.1007/BF00168222>
- Okal, E. A., Reymond, D., & Hébert, H. (2013). From earthquake size to far-field tsunami amplitude: Development of a simple formula and application to DART buoy data. *Geophysical Journal International*, 196(1), 340–356.
- Piatanesi, A., & Lorito, S. (2007). Rupture process of the 2004 Sumatra-Andaman earthquake from tsunami waveform inversion. *Bulletin of the Seismological Society of America*, 97(1 A SUPPL), 223–231. <https://doi.org/10.1785/0120050627>
- Satake, K. (1987). Inversion of tsunami waveforms for the estimation of a fault heterogeneity: Method and numerical experiments. *Journal of Physics of the Earth*, 35(3), 241–254. <https://doi.org/10.4294/jpe1952.35.241>
- Satake, K., Fujii, Y., Harada, T., & Namegaya, Y. (2013). Time and space distribution of coseismic slip of the 2011 Tohoku earthquake as inferred from tsunami waveform data. *Bulletin of the seismological society of America*, 103(2B), 1473–1492.
- Satake, K., Wang, K., & Atwater, B. F. (2003). Fault slip and seismic moment of the 1700 Cascadia earthquake inferred from Japanese tsunami descriptions. *Journal of Geophysical Research*, 108(B11), 2535. <https://doi.org/10.1029/2003JB002521>
- Schmalzle, G. M., McCaffrey, R., & Creager, K. C. (2014). Central Cascadia subduction zone creep. *Geochemistry, Geophysics, Geosystems*, 15, 1515–1532. <https://doi.org/10.1002/2013GC005172>
- Tanioka, Y., Yudhicara, Kususose, T., Kathiroli, S., Nishimura, Y., Iwasaki, S. I., & Satake, K. (2006). Rupture process of the 2004 great Sumatra-Andaman earthquake estimated from tsunami waveforms. *Earth, Planets and Space*, 58(2), 203–209. <https://doi.org/10.1186/BF03353379>
- Titov, V., Rabinovich, A. B., Mofjeld, H. O., Thomson, R. E., & González, F. I. (2005). The global reach of the 26 December 2004 Sumatra tsunami. *Science*, 309(5743), 2045–2048. <https://doi.org/10.1126/science.1114576>
- Vigny, C., Socquet, A., Peyrat, S., Ruegg, J. C., Metois, M., Madariaga, R., et al. (2011). The 2010 Mw 8.8 Maule megathrust earthquake of central Chile, monitored by GPS. *Science*, 332(6036), 1417–1421. <https://doi.org/10.1126/science.1204132>
- Wei, Y., Newman, A. V., Hayes, G. P., Titov, V. V., & Tang, L. (2014). Tsunami forecast by joint inversion of real-time tsunami waveforms and seismic or GPS data: Application to the Tohoku 2011 tsunami. *Pure and Applied Geophysics*, 171(12), 3281–3305. <https://doi.org/10.1007/s00024-014-0777-z>
- Williamson, A., Newman, A., & Cummins, P. (2017). Reconstruction of coseismic slip from the 2015 Illapel earthquake using combined geodetic and tsunami waveform data. *Journal of Geophysical Research: Solid Earth*, 122, 2119–2130. <https://doi.org/10.1002/2016JB013883>
- Witter, R. C., Kelsey, H. M., & Hemphill-Haley, E. (2003). Great Cascadia earthquakes and tsunamis of the past 6700 years, Coquille River estuary, southern coastal Oregon. *Geological Society of America Bulletin*, 115(10), 1289–1306. <https://doi.org/10.1130/B25189.1>
- Yue, H., Lay, T., Rivera, L., An, C., Vigny, C., Tong, X., & Soto, J. C. B. (2014). Localized fault slip to the trench in the 2010 Maule, Chile Mw = 8.8 earthquake from joint inversion of high-rate GPS, teleseismic body waves, InSAR, campaign GPS, and tsunami observations. *Journal of Geophysical Research: Solid Earth*, 119, 7786–7804. <https://doi.org/10.1002/2014JB011340>
- Romano, F., Piatanesi, A., Lorito, S., D'Agostino, N., Hirata, K., Atzori, S., et al. (2012). Clues from joint inversion of tsunami and geodetic data of the 2011 Tohoku-oki earthquake. *Scientific Reports*, 2(1), 1–8. <https://doi.org/10.1038/srep00385>